

High-Power Radiation at 1 THz in Silicon: A Fully Scalable Array Using a Multi-Functional Radiating Mesh Structure

Zhi Hu , *Student Member, IEEE*, Mehmet Kaynak, and Ruonan Han, *Member, IEEE*

Abstract—We introduce a highly scalable architecture of coherent harmonic oscillator array for high-power and narrow-beamwidth radiation in the mid-terahertz (THz) band. The array consists of horizontal and vertical slotlines (i.e., slot mesh) located at the boundaries between oscillator elements. Through such a structure, the following operations are achieved simultaneously: 1) maximum oscillation power at fundamental frequency f_0 ; 2) precise synchronization of the oscillation phase among elements; 3) cancellation of the radiation at f_0 , $2f_0$, and $3f_0$; and 4) efficient radiation and power combining at $4f_0$. The resultant compact design fits into the optimal radiator pitch of $\lambda_{4f_0}/2$ (half wavelength) for the suppression of sidelobes, hence enabling implementation of high-density THz arrays. In particular, an array prototype of 42 coherent radiators (with 91 resonant antennas) at 1 THz is presented using the IHP S13G2 130-nm SiGe process. The chip occupies only 1-mm² area and consumes 1.1 W of dc power. The measured total radiated power and the effective isotropically radiated power are 80 μ W and 13 dBm, respectively.

Index Terms—Harmonic oscillator, multi-functional circuit, scalable radiating array, SiGe, silicon, terahertz (THz) source.

I. INTRODUCTION

TERAHERTZ (THz) spectrum, commonly defined to be between 0.3 and 3 THz, possesses properties that are critical to chip-based sensing applications; particularly, in the *mid-THz* range (around 1 THz), important applications include, but are not limited to, high-resolution THz imaging [1], vibrational spectroscopy of large bio-molecules (e.g., DNA) [2], rotational spectroscopy for trace gas analysis [3], [4], and sub- μ m-precision vibrometry based on Doppler effect [5]. However, since the frequency lies well beyond f_{\max} of all silicon-based transistors, generating high-power radiation in this band is very challenging. This has been clearly reflected in previous publications (see Fig. 1). In [6] and [7], using active multipliers based on SiGe heterojunction

Manuscript received August 28, 2017; revised November 16, 2017; accepted December 14, 2017. Date of publication January 11, 2018; date of current version April 23, 2018. This paper was approved by Guest Editor Osama Shanaa. This work was supported in part by the National Science Foundation, in part by Analog Devices, Inc., in part by the Singapore-MIT Research Alliance, in part by the MIT/MTL GaN Energy Initiative, and in part by the MIT Center of Integrated Circuits and Systems. (*Corresponding author: Zhi Hu.*)

Z. Hu and R. Han are with the Department of Electrical Engineering and Computer Science, Massachusetts Institute of Technology, Cambridge, MA 02139 USA (e-mail: zhihu@mit.edu).

M. Kaynak is with the Leibniz-Institut für innovative Mikroelektronik (IHP), 15236 Frankfurt (Oder), Germany.

Color versions of one or more of the figures in this paper are available online at <http://ieeexplore.ieee.org>.

Digital Object Identifier 10.1109/JSSC.2017.2786682

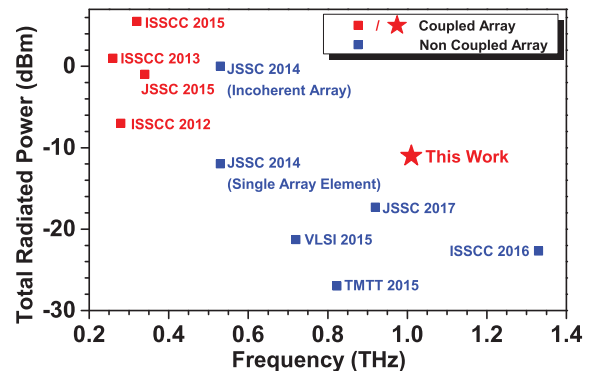


Fig. 1. Comparison of output power and architectures of sub- and mid-THz radiators in silicon (see [7]–[10], [12]–[16]).

bipolar transistors (HBTs), waves at 0.82 and 1 THz are generated, respectively, with an effective isotropically radiated power (EIRP) of -37 and -17 dBm, respectively. In [8] and [9], using frequency multipliers based on MOS varactors, waves at 0.73 and 1.33 THz are generated with an EIRP of -22 and -13 dBm, and a total radiated power (P_{rad}) of -21 and -23 dBm, respectively. In [10], an active multiplier with a non-linear feedback loop generates 0.92-THz radiation with an EIRP of -10 dBm and P_{rad} of -17 dBm. In [11], using an ultra-fast pulse generator, a circuit generates a broadband comb spectrum, in which the radiation near 1 THz has an EIRP of ~ -70 dBm.

To further increase the radiated power, a multi-antenna/element source with free-space power combining is preferred. Moreover, according to antenna array theories [17], to minimize grating lobes in the radiation pattern, spacing between antennas should be half wavelength ($\lambda/2$) in both axes of the array. Therefore, in a given chip area, a large number of radiators can be implemented when the operation frequency is high, hence a very narrow output beam [17]. As shown in Fig. 2, the radiator density at 1 THz should ideally reach about 100/mm² and enable radiation beamwidth of only a few degree with a practical chip size [18]. These properties effectively compensate the high-frequency path loss and enhance the spatial resolution in imaging and material-probing applications.

However, large-scale radiator arrays in mid-THz range were not reported previously (illustrated in Fig. 1). The sources in [9] and [10] have two antennas fed by a single input with a power splitter; such a solution, although offering higher EIRP,

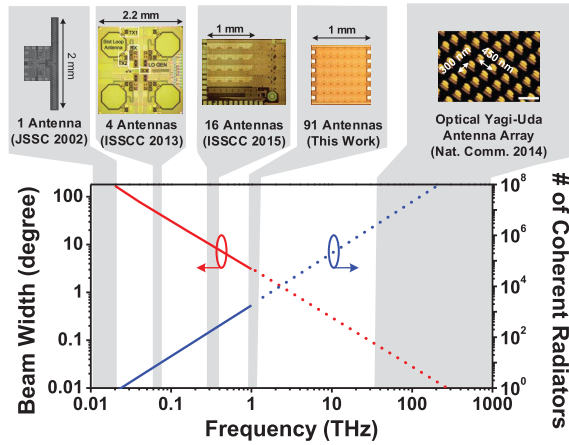


Fig. 2. Estimation of the number of coherent radiators integrated on a 10-mm² chip area and the corresponding beamwidth across the RF-to-optical spectrum. In the calculation of the wavelength, a dielectric environment with an equivalent relative dielectric constant of 2 is assumed. Works shown are [12], [13], [20], and [21].

does not increase the total radiated power. In [7], four antennas are placed at the chip center and fed by four multiplier chains at the periphery of the chip. It is noteworthy that all of these configurations are not scalable due to their *centralized* nature: for a large-size array, the complexity and loss of the signal-distribution network increase exponentially. Even if these multiplier arrays are realized, the much larger required input power at low-THz frequency will be inaccessible on chip.

In comparison, a coupled coherent harmonic oscillator array is more effective and has been extensively used in sub-THz radiators [12], [13], [16], [19]. Due to its self-sustaining nature and synchronization mechanism through inter-unit mutual coupling (hence a *decentralized* scheme), it is expected to have better scalability. There are, however, two critical challenges that have hindered the implementation of large-scale coupled radiator array previously.

A. Size of Radiator Unit

Due to the short wavelength at 1 THz in the inter-metal-layer dielectrics of standard chip processes, the available area for a radiating unit is merely $100 \times 100 \mu\text{m}^2$ ($\lambda_{f_{\text{out}}}/2 \approx 100 \mu\text{m}$). Meanwhile, within such a limited space, each unit should contain several non-trivial components as follows.

- 1) A harmonic oscillator running at a fraction of the output frequency ($f_0 = f_{\text{out}} \div N$, $N = 2, 3, \dots$), which requires a large fundamental resonator with a size of about $N \cdot \lambda_{f_{\text{out}}}/4$. Since f_{max} of mainstream silicon transistors is below 0.5 THz [22], N is 4 or greater in practice.
- 2) A resonant antenna, which is typically $\lambda_{f_{\text{out}}}/2$ in length (e.g., dipole or slot antenna). Other antennas, such as patch antenna, occupy even larger 2-D area, leaving very little space for other components [16].
- 3) Filters to suppress undesired radiation of low-order harmonics and to recycle their power for up-conversion to $N \cdot f_0$. Prior works utilize multi-phase interference at the central power-combining node [see Fig. 3(a)], but it requires N sub-oscillators (hence large area) and leads

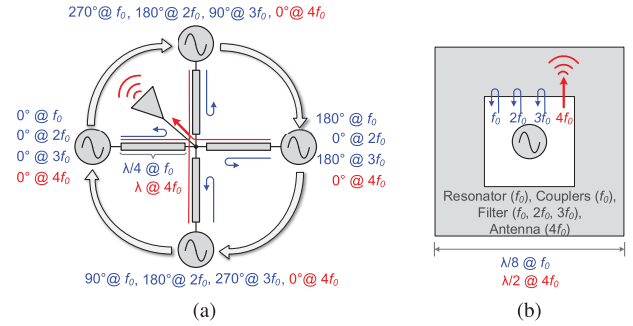


Fig. 3. (a) Conventional fourth-harmonic oscillator and (b) compact fourth-harmonic oscillator presented in this paper using a multi-functional EM structure.

to long [$\lambda_{f_{\text{out}}}$ in Fig. 3(a)] and lossy path for the output signal.

- 4) Four frequency/phase couplers to synchronize with neighboring units in all four directions. Previous schemes in THz circuits are based on linear coupling [14] and ring coupling [13], which are unable to scale to large 2-D arrays.

B. Phase Mismatch in 2-D Coupling

The coupling among oscillators is based on injection locking. However, process–voltage–temperature (PVT) variations of these oscillators lead to non-zero phase difference of their waveforms in a steady state. For a simplified system of two coupled oscillators with free-running oscillation frequencies of ω_0 and $\omega_0 + \Delta\omega$, the phase shift $\Delta\theta$ as the result of mutual injection locking is governed by Adler's equation at the steady state ($d\theta/dt = 0$) [23]

$$\Delta\theta = \arcsin\left(\frac{Q}{\omega_0} \cdot \frac{I_{\text{osc}}}{I_{\text{inj}}} \cdot \Delta\omega_0\right) \quad (1)$$

where Q is the quality factor of the resonators, and I_{osc} and I_{inj} are the ac currents in the resonator, respectively, from the oscillator itself and the injection of another oscillator. Suppose $Q = 10$, $\omega_0 = 250$ GHz, and $I_{\text{osc}}/I_{\text{inj}} = 3$, even a small frequency mismatch $\Delta\omega$ of 1 GHz causes large $\Delta\theta$ of 7° , which corresponds to a phase mismatch $\Delta\theta_{4f_0}$ of 28° for the fourth-harmonic output. Since PVT variations in a large array usually follow gradient patterns [24], the above phase shift could potentially be distributed across the array and cause severe tilting of the combined output beam. An ultra-strong coupling approach is, therefore, indispensable.

This paper presents a new architecture applicable for a large-size coupled array in the mid-THz band. In particular, such an architecture is enabled by a highly compact, multi-functional radiator structure [see Fig. 3(b)] that addresses all the aforementioned challenges. A 1-THz 2-D radiating array consisting of 6×7 coherent units and 91 resonant antennas is prototyped using the IHP 130-nm SiGe HBT process. The measured total radiated power and the EIRP of the chip are $80 \mu\text{W}$ and 13 dBm (20 mW), respectively.

This paper provides the detailed descriptions of the 1-THz chip originally reported in [25], with an additional quantitative analysis on inter-element oscillator coupling.

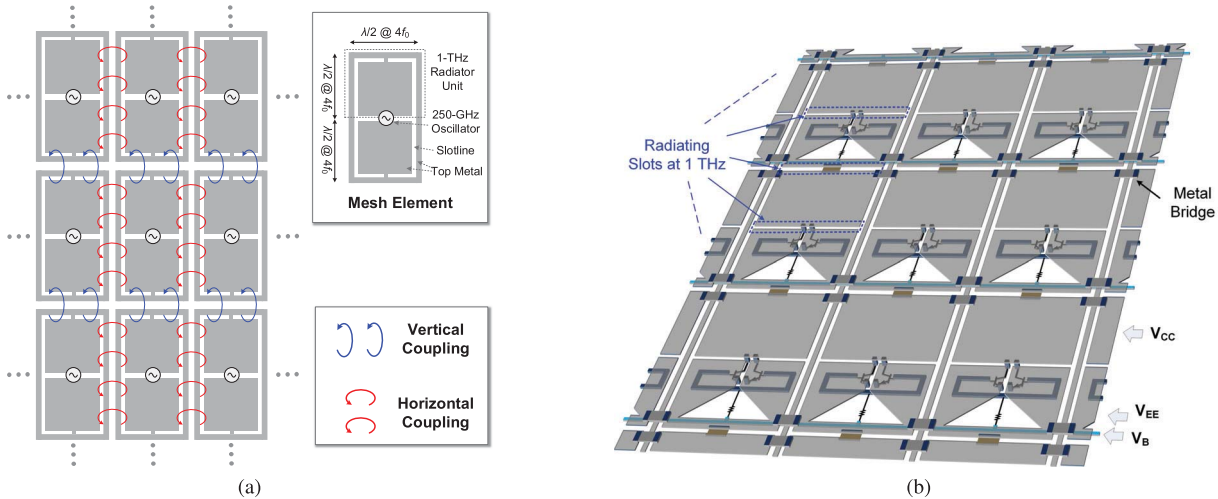


Fig. 4. 3×3 element array. (a) Basic conceptual block diagram. (b) Physical implementation, including the dc bias connections.

Moreover, extensive discussions on radiation cancellation/combining, dc bias, and array boundaries are also presented. The remainder of this paper is organized as follows. In Section II, we give an overview of the array. In Section III, we introduce the design of a single element. In Section IV, we explain how to form the array using the elements, and how coupling and radiation take effect with the presence of multiple elements. In Section V, we show the experimental results and compare this paper with other state of the arts. Finally, a conclusion is given in Section VI.

II. OVERVIEW OF THE ARRAY ARCHITECTURE

In this section, we present the architecture of the array, which is based on a square slotline mesh structure. In Fig. 4, a 3×3 element array (expandable in both horizontal and vertical directions) is shown. Each mesh *element* consists of two *radiating units*, and each unit has a square slot ring implemented in the top metal layer of the chip. At the horizontal center of the mesh element, the two radiating units share two slotlines, which are driven by a 250-GHz oscillator. As is described in detail in Sections III and IV, once the oscillation starts, these slotlines guide the generated waves to the upper and lower units within each array element, and simultaneously perform the following functions:

- 1) optimization for the fundamental oscillation at 250 GHz (f_0) and harmonic generation at $4f_0$;
- 2) coupling and synchronization for the oscillation among neighboring mesh elements;
- 3) cancellation of the undesired radiation at f_0 , $2f_0$, and $3f_0$;
- 4) backside radiation¹ at $4f_0$ (1 THz) through *all* horizontal slots of the mesh.

For strong inter-element coupling, the array elements are placed like tiles (see Section IV). In particular, the two

¹Although front-side radiation has advantages in terms of packaging, we use backside in this design. With backside radiation, we are able to reduce the footprint of antennas (compared with patch antennas) in the limited area. Also, as will be seen later, slot antennas are an integral part of branched resonators, which makes each element multi-functional.

top/bottom horizontal slots of vertically adjacent elements even *merge* and form a single slot. As a result, although three horizontal slot pairs are shown in the mesh element in Fig. 4(a), there are, in fact, *two* radiating slot pairs per element on average in the actual implemented array structure, as shown in Fig. 4(b).

Last, it is also important to note that each radiator unit has a size of about $\lambda/2 \times \lambda/2$ at 1 THz [see Fig. 4(a)]. Therefore, the pitch of the horizontal radiating slot pairs (acting as dipole slot antennas, see Section IV) is the optimal value ($\lambda_{f_{out}}/2$) in both horizontal and vertical directions, meeting one of the stringent requirements of large-scale active arrays outlined in Section I.

III. RADIATING MESH ELEMENT: DESIGN AND OPERATIONS AT THE FUNDAMENTAL FREQUENCY

In this section, part of a circuit-electromagnetic (EM) co-design approach for the radiating mesh element is shown, with the major focus on the principles of fundamental oscillation at 250 GHz (f_0). Although an individual element effectively radiates 1-THz wave regardless of being inside an array or not, most of the operations at $2f_0$ to $4f_0$ benefit from the interactions of adjacent elements inside an array configuration. Details related to those are, therefore, presented in Section IV, where inter-element coupling and array formation are introduced.

The EM structure of a single mesh element is shown in Fig. 5(a). To understand its operations, we point out that, our circuit widely adopts highly distributed slot structures, where the enclosed electromotive force is non-zero due to the time-varying magnetic flux; therefore, *the concept of “ground” can only be defined locally for each individual distributed structure (e.g., transmission line)*. In fact, even if two “local grounds” are physically associated with one piece of metal, they should not be considered to be electrically connected. For that reason, some slots are illustrated as two-conductor transmission lines (with explicit local ground).

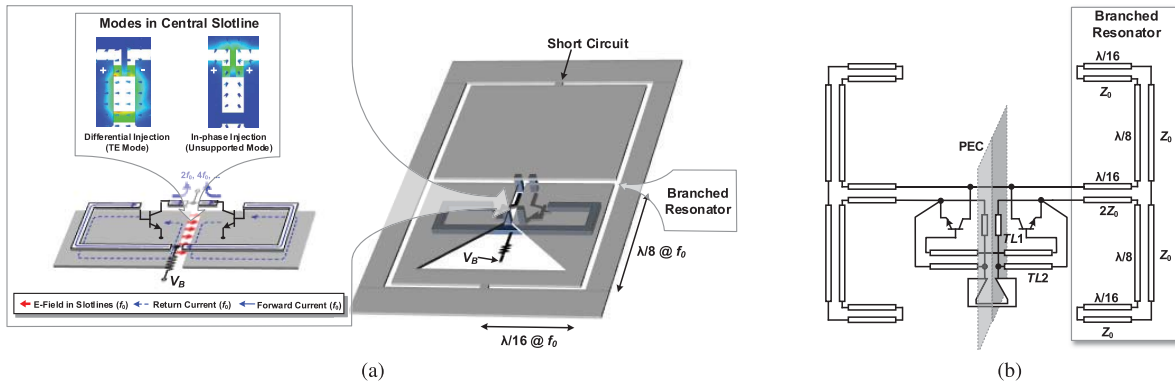


Fig. 5. (a) Structure of a single element. The inset on the left shows the 1-THz oscillator, and the inset on the right shows the branched resonator. The signal trace of the self-feeding microstrip lines, in the actual layout, is implemented using stacked Metal 2-4. The structure on the left inset is a flipped representation for visual clarity. (b) Equivalent circuit of the array element at 250 GHz.

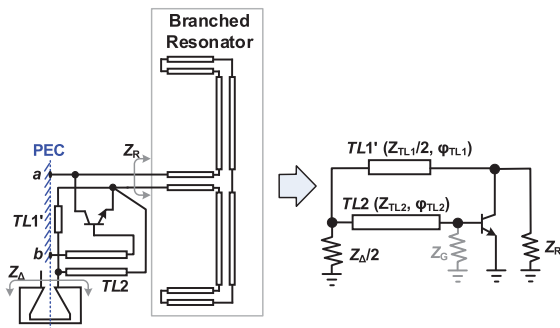


Fig. 6. Transformation of the half-circuit equivalent of Fig. 5(b) to a standard self-feeding oscillator topology [13] (in which $Z_B = \infty$).

Based on such principles, the equivalent circuit schematic of the array element is shown in Fig. 5(b), which consists of a differential oscillator core and a pair of branched resonators.

A. 250-GHz Oscillator Core

The oscillator core is located at the lower radiating unit of each element [see Fig. 5(a)]. It can be regarded as two identical oscillators coupled together [see Fig. 5(b)], with each one composed of: 1) an HBT transistor and a short vertical slotline ($TL1$) connecting to the emitter and 2) a microstrip line ($TL2$) connecting $TL1$ with the transistor base.

First, for differential-mode oscillation, note that due to symmetry, all electrical-field vectors in the oscillator structure is normal to a central perpendicular plane [see Fig. 5(b)]. This plane is thus a virtual perfect conductor plane [perfect electrical conductor (PEC)]. Accordingly, the oscillator can then be analyzed through its half-circuit equivalent, as shown in Fig. 6. The PEC and one conductor plane of $TL1$ form a new slotline $TL1'$ that connects Nodes a and b .² Since the field distribution of this $TL1'$ is identical to half of that in $TL1$ [shown in Fig. 5(a)], the relationships of their impedances and electrical lengths are $Z_{TL1'} = 0.5Z_{TL1}$ and $\varphi_{TL1'} = \varphi_{TL1}$, respectively. Next, the triangle opening in the

²Although a PEC does not have resistance, these two nodes are still not directly connected. Instead, this PEC should be considered as a conductor of a transmission line.

lower metal plane, essentially a tapered slot resonator, provides a broadband open-circuit termination [26]. Its role is to enclose the slot $TL1$ while not affecting the wave propagation inside $TL1$; meanwhile, the oscillation frequency is only determined by the branched resonators, not this broadband opening. In Fig. 6, half of the large impedance ($Z_{\Delta}/2$) of the triangle opening is connected to the equivalent self-feeding oscillator.

As shown in Fig. 6, a feedback path at f_0 is created from the collector to the base through $TL1'$ and $TL2$. In practice, φ_{TL1} is very short, and $Z_{TL1'}/2$ equals to Z_{TL2} . This is then a self-feeding oscillator originally presented in [13], where the feedback loop greatly destabilizes the transistor, and enables strong oscillation.³ Previous works [27], [28] have shown that to maximize the oscillation power of a transistor, the complex voltage gain A of the transistor should have a phase of

$$\angle A = \angle - (y_{21} + y_{12}^*) \quad (2)$$

where y_{ij} is the element of the transistor Y -parameter matrix. This condition compensates the THz signal delay inside the transistor, which is caused by the finite transit time and a base-to-collector feedforward current through C_{μ} [13]. To meet the requirement in (2), the total length $\varphi_{TL1} + \varphi_{TL2}$ of the self-feeding transmission line should follow [13]:

$$\varphi_{TL1} + \varphi_{TL2} = \arcsin \left(\frac{\text{Im}(A)}{Z_{TL2} \cdot \text{Re}(y_{11} + A \cdot y_{12})} \right). \quad (3)$$

Once the relative length $\varphi_{TL1} + \varphi_{TL2}$ (in degree) is obtained, the absolute physical length can be then derived with the oscillation frequency determined by the branched resonator (see Section III-B). Note that a complete self-feeding topology also contains a reactive termination at the base (Z_B in Fig. 6), which does not exist in our oscillator. Fortunately, Z_B can normally be eliminated by choosing a proper $Z_{TL} - \varphi_{TL}$ combination. After iterations between this linear theory and

³An alternative simplistic way to understand the self-feeding topology is to view it as a “high-frequency version” of the three-point Colpitts oscillator [27], where the inductor (lumped) is replaced with a transmission line (distributed). However, note that the focus of self-feeding oscillator is the complex voltage gain from base to collector, which is typically not considered in a Colpitts oscillator design.

large-signal simulation, we choose $|A| = 2.2$, $Z_{TL2} = 40 \Omega$, and $\varphi_{TL2} = 34^\circ$.

By symmetry, an in-phase oscillation may also exist. Fortunately, this undesired mode is effectively suppressed. Because the TM wave associated with this excitation mode inside $TL1$ is not supported at 250 GHz, as shown by the HFSS simulation in Fig. 5(a).

Given that the collector voltages of the two HBTs at $2f_0$ and $4f_0$ are also in-phase, these harmonic waves are then blocked by the slotline $TL2$ for the same reason. So they do not travel back to the *lossy* bases of transistors through the oscillation feedback loop. In other words, the generation efficiency of harmonic signals is improved.

B. Branched Resonator

A pair of branched resonators shown in Fig. 5(a) are used for regulating the oscillation frequency at 250 GHz. Each resonator is a partially shunt combination of two quarter-wave slot transmission lines with an impedance of Z_0 and short terminations at their far ends [see Fig. 5(b)]. When the two branches of the resonator are combined at the central T-junction, the signal current does not change, but the voltage is doubled; as a result, the impedance of the shunt section of the resonator is designed to be $2Z_0$, in order to avoid internal wave reflections. In Section IV, we will show how this special resonator geometry assists the inter-coupling and radiation interference among multiple elements.

In our design, the slot width of the branched section of the resonator is $4 \mu\text{m}$, which gives an impedance Z_0 of 61Ω . The top inset of Fig. 7 shows the simulated impedance when a differential excitation is applied to the collector-source ports of HBTs (and without the presence of $TL2$), which is approximately

$$Z_{R,\text{total}} \approx (Z_{R,\text{left}} + Z_{R,\text{right}}) // Z_{\Delta} = 2Z_R // Z_{\Delta} \quad (4)$$

where Z_R and Z_{Δ} are defined in Fig. 6.⁴ The approximation is based on the fact that the vertical slot $TL2$ between Z_R and Z_{Δ} is very short. For the 250-GHz resonance, the simulated quality factor of the resonator is ~ 17 .

C. Simulation Results of the Fundamental Oscillation

Using the design parameters provided in this section, the simulated dc power consumption of the oscillator is 25.2 mW from a 1.8-V supply.⁵ Meanwhile, the simulated power injected into the branched resonator from the transistors, at $4f_0$ (~ 1 THz), is $3.4 \mu\text{W}$. Here, the impedance of the resonator pair at $4f_0$, under in-phase excitation from the two HBTs, is simulated $(31 + j \cdot 23 \Omega)$, shown in the bottom inset of Fig. 7) and matched to the transistors. In Section IV, we will show how the 1-THz signal is radiated from the branched resonators.

⁴ $Z_{R,\text{left}}$ and $Z_{R,\text{right}}$ share the same current path, and their ports are connected with the differential outputs of the oscillator pair, so their impedances are in series. Z_{Δ} is also connected to the output of the oscillator pair, but its current path is independent of the current path of the branched resonators, so its impedance is in shunt with $(Z_{R,\text{left}} + Z_{R,\text{right}})$.

⁵The power supply voltage is slightly higher than the 1.7-V BV_{CEO} of the HBTs. However, since the HBT bases in the circuit are not open-terminated, the actual breakdown voltage is higher than 1.8 V.

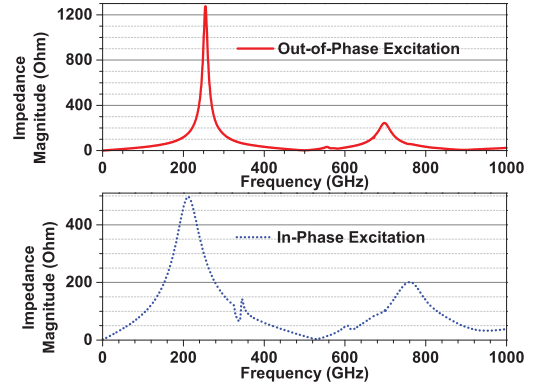


Fig. 7. EM simulation of the resonator impedance with out-of-phase excitation (for signals at f_0 and $3f_0$) and in-phase excitation for signals at $2f_0$ and $4f_0$.

IV. LARGE-SCALE ARRAY: A RADIATING SLOT MESH

In this section, we discuss the multi-fold functions of the branched resonators when forming a large-scale array.

A. Inter-Element Frequency/Phase Synchronization

The details of the evolution from a single element (see Fig. 5) to a radiating mesh are shown in Fig. 8. Next, we discuss how the inter-element coupling is achieved for frequency/phase synchronization, which happens via the slotlines on all four boundaries of each element.⁶

1) *Horizontal Coupling*: For two horizontally adjacent elements, their branched resonator slots share the same outer metal plane, which eventually evolves to a narrow metal strip. Meanwhile, a metal bridge is used to enforce the equal-potential condition for the other two metal planes of the two slots. In this way, the two vertical sections of the branched resonators form a standard co-planar waveguide (CPW), in which the electrical fields of the two slots are oriented to *opposite* directions. Note that only standing waves exist, and at steady state, the collector voltages (see Fig. 8) of the two oscillators satisfy $V_1 = -V_2 = -V_3 = V_4$. We also note that the CPW interface (for horizontal coupling) has the same voltage as the associated slot in a single element, but twice of the current. Hence, its characteristic impedance is designed to be half of Z_0 in Fig. 5. Such an adjustment keeps the operations introduced in Section III unchanged.

2) *Vertical Coupling*: For two vertically adjacent elements, their horizontal slots on the top/bottom boundaries are directly merged into a single slot (see Fig. 8). As explained in Fig. 5(b), only quasi-TE mode is supported in the merged slot so that the two elements are only allowed to be coupled with a mode, where electrical fields associated with the original horizontal slots of these two elements are oriented to the *same* direction. Therefore, the following relationship holds: $V'_1 = -V'_2 = V'_3 = -V'_4$, which is in contrast with the horizontal coupling scheme introduced previously. In Section IV-C, we show

⁶When the phase/frequency of signals at f_0 from different elements are synchronized, the phase/frequency at other harmonics are synchronized as well. Therefore, the following discussion focuses on synchronizations at f_0 .

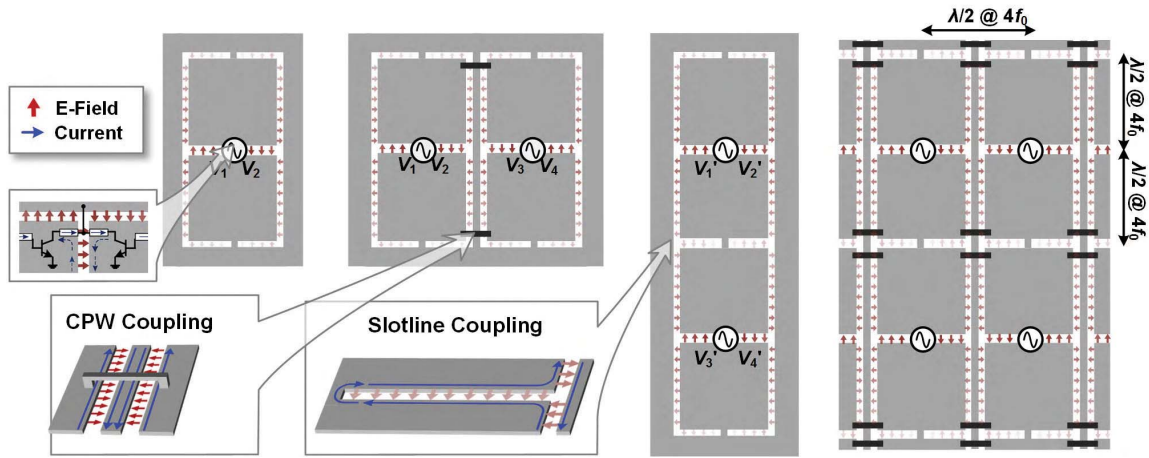


Fig. 8. Array forming from a single element. Field distributions at f_0 are shown in 1×1 , 1×2 , 2×1 , and 2×2 cases to illustrate the coupling among the horizontal and vertical elements.

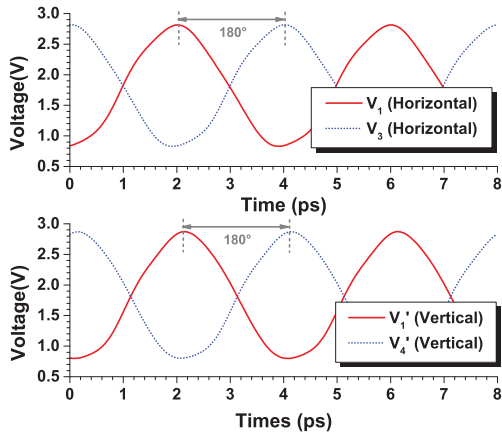


Fig. 9. Simulated waveforms of two coupled oscillating elements. (a) V_1 and V_3 and (b) V_1' and V_4' in Fig. 8.

that this choice leads to a multi-harmonic interference that selectively facilitates the radiation at $4f_0$.

Although by symmetry, the out-of-phase coupling mode of the oscillators also exists, it is completely suppressed in practice, because in this undesired mode, the merged slot, which is unable to support the associated central-symmetric TM wave, presents an open-circuit termination. In this case, each branched resonator becomes a 67.5° open stub and presents a 26-fF capacitance to the collector of each oscillator. The oscillation with this mode is, therefore, unable to start. Last, note that the merged slot has the same current as that in the slot of a single element, but twice of the voltage. Therefore, the characteristic impedance of the merged slot is designed to be $2Z_0$ (i.e., larger slot width).

As a result of the above-mentioned coupling schemes, in our EM simulations for multiple coupled elements inside the mesh, the left/right boundaries are set as perfect magnetic conductors, whereas the top/bottom boundaries are set as PECs. The generated S -parameters are used in the circuit simulations of horizontal/vertical coupling between oscillators, and the resultant waveforms are shown in Fig. 9. Note that the phase relationships match our previous analysis in this section.

B. Phase Mismatch in Coupling: A Quantitative Analysis

Up to this point, all analyses and simulations are based on the assumption that no mismatch between oscillators exists. Next, we derive a model to study the strength of injection locking and the resultant phase mismatch with the variation of free-running oscillation frequencies in the array elements.

First, for the case of horizontal coupling, the model is based on the schematic shown in Fig. 10(a): two oscillators are coupled by a network consisting of two 90° -long transmission lines (i.e., branched resonators) with a shunt connection at an electrical length of φ away from the oscillator cores.

We assume that the tanks of the two oscillators have resonance frequencies of ω_1 and ω_2 ($\Delta\omega = |\omega_1 - \omega_2| \ll \omega_1$), quality factors of Q_1 and Q_2 ($Q_1 \approx Q_2 = Q$), and shunt resistances of $R_{\text{tank},1}$ and $R_{\text{tank},2}$ ($R_{\text{tank},1} \approx R_{\text{tank},2} = R_{\text{tank}}$). Meanwhile, the voltages across the two tanks, in the synchronized steady state with a common oscillation frequency of ω_0 , are expressed as

$$\begin{cases} v_1(t) = (A_0 + \Delta A) \cdot e^{j(\omega_0 t + \Delta\theta)} \\ v_2(t) = (A_0 - \Delta A) \cdot e^{j(\omega_0 t - \Delta\theta)} \end{cases} \quad (5)$$

where the amplitude mismatch ΔA and the phase mismatch $\Delta\theta$ are assumed to be small. Following the derivations in the Appendix, which decompose the circuit operation into common-mode and differential components [see Fig. 10(a)], we are able to get the phase difference between $v_1(t)$ and $v_2(t)$ (when $d\Delta\theta/dt = 0$):

$$2\Delta\theta = 2 \arctan \left(\frac{\omega_1 - \omega_2}{\omega_0} \cdot Q \cdot \frac{Z_0^2 \tan^2 \varphi}{R_{\text{tank}}^2} \right). \quad (6)$$

We note that, the phase difference $2\Delta\theta$ only manifests itself inside the two stubs (Z_0, φ) between the oscillators and the short-circuit connection; it decreases from $2\Delta\theta$ at the oscillator core to 0° at the short-circuit connection. Beyond the short-circuit connection, no phase difference exists in the remaining $90^\circ - \varphi$ section of the branched resonators. For the coupling in the horizontal direction, the parameter φ in (6) is

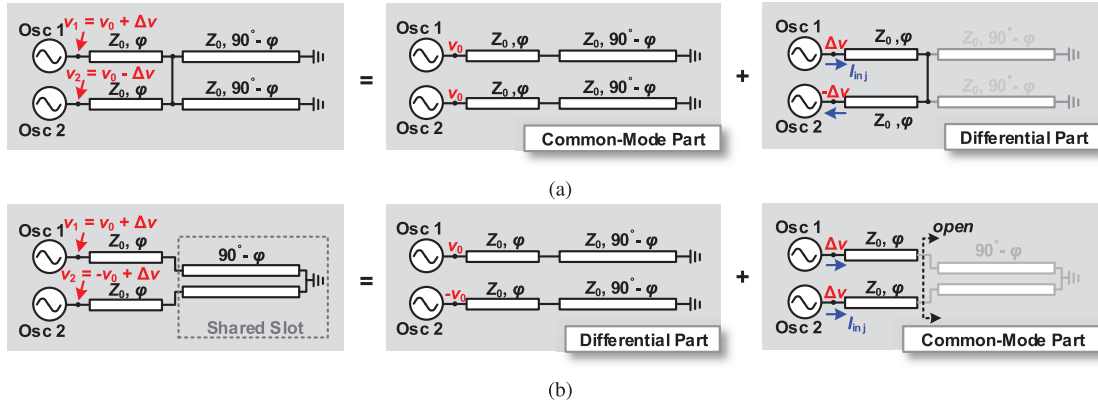
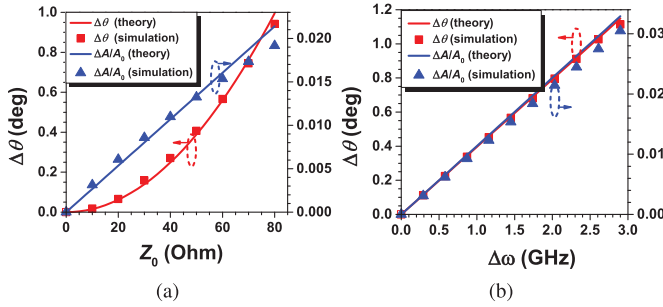


Fig. 10. Models and schematic decompositions for (a) horizontal coupling and (b) vertical coupling.


 Fig. 11. Calculated and simulated results of $\Delta\theta$ and $\Delta A/A_0$ for two coupled 250-GHz self-feeding oscillators using the branched resonator network. (a) $\Delta\omega = 1.5$ GHz and $\varphi = \pi/8$. (b) $Z_0 = 60 \Omega$ and $\varphi = \pi/8$.

close to $\pi/8$.⁷ To verify the model, we perform circuit simulations, where two 250-GHz self-feeding oscillators are coupled via the branched resonator network. As shown in Fig. 11, the phase/amplitude mismatch predicted by our model well matches the simulation results.

A similar model and an analytical approach also apply to the vertical coupling. Here, although the two oscillators are coupled in-phase, the voltages presented at the two resonator slots are out-of-phase (see Fig. 8). For this desired coupling mode, each oscillator shows a quarter-wavelength transmission line [see Fig. 10(b)]. But for the undesired common-mode coupling, each oscillator shows an *open-circuit* stub with a length of φ . Therefore, the only correction needed to be made to the previous model is that the injected current in (15) becomes

$$i'_{inj,i} = \mp \Delta v / (-j Z_0 \cot \varphi) \quad (i = 1, 2) \quad (7)$$

where Δv is now the amplitude difference of the two *differential* oscillator voltages, i.e., $\Delta v = (v_1 + v_2)/2$.

⁷The two vertical slot transmission lines at $\varphi = \pi/8$ to $3\pi/8$ are tightly coupled, with an even-mode characteristic impedance of Z_{even} (for the desired CPW coupling) much higher than that of the characteristic impedance Z_{odd} in the undesired odd-coupling mode. In our case, Z_{even} is made close to Z_0 to minimize reflections of common-mode signals, while Z_{odd} is only about $Z_0/5$. For out-of-phase coupling, the differential impedance looking into the resonator at $\varphi = \pi/8$ (i.e., $j Z_{\text{odd}}$) is, therefore, very small. Although the metal bridge is physically located near $\varphi = 3\pi/8$, the ultra-tight coupling makes equivalent φ to be close to $\pi/8$.

The phase mismatch in the vertical direction is then

$$2\Delta\theta' = 2 \arctan \left(\frac{\omega_1 - \omega_2}{\omega_0} \cdot Q \cdot \frac{Z_0^2 \cot^2 \varphi}{R_{\text{tank}}^2} \right). \quad (8)$$

For the vertical coupling in our case, φ is $3\pi/8$. Interestingly, since $\tan(\pi/8) = \cot(3\pi/8)$, (6) and (8) give the same result, and Fig. 11(b) can be used for the phase and amplitude mismatch in both the horizontal and vertical directions.

It can be seen from (6) and (8) that by decreasing Z_0 and increasing R_{tank} , we are able to decrease $\Delta\theta$ and $\Delta\theta'$ and thus achieve strong coupling.

C. Selective Radiation at $4f_0$ Using Near-Field Interference

Selective radiation using slot structures can be traced back to [29]. The input signal may excite either radiative or non-radiative mode depending on the phase relationship of standing waves in the different sections of a slot antenna. This property was further exploited in [14] to radiate only the second-harmonic ($2f_0$) signal of an oscillator. Nevertheless, there has not been a selective antenna for radiation at $4f_0$.

The geometry and dimension of the branched resonator pair in our 1-THz radiator design are designed to provide the following function: it has a radiative mode and a non-radiative mode and the radiative mode is only excited at $4f_0$. Details on this operation are explained using the electrical-field distribution of standing waves at f_0 to $4f_0$, as shown in Fig. 12. First, Fig. 12 (a)–(d) shows that, at all frequencies, next to each vertical slotline, there is another vertical slotline from the horizontally adjacent element. As discussed before, these two slotlines carry out-of-phase fields, and thus, they do not radiate. Due to this reason, in the remainder of this section, only the radiation properties of the *horizontal* slotlines are discussed. The following analyses are based on the polyharmonic standing-wave patterns in slotline $\overline{A_i B_i C_i D_i}$ ($i = 1, 2, 3, 4$), of which the lengths are close to $(1/4)\lambda$, $(1/2)\lambda$, $(3/4)\lambda$, and λ at f_0 , $2f_0$, $3f_0$, and $4f_0$, respectively.

At f_0 [see Fig. 12(a)], due to the differential oscillation, waves injected into the left and right branched resonators are out-of-phase; we denote it as the *odd* mode of the branched resonator pair. In the odd mode, for each of the following slotline pairs— $(\overline{A_1 B_1}, \overline{A_2 B_2})$, $(\overline{D_1 C_1}, \overline{D_2 C_2})$, and

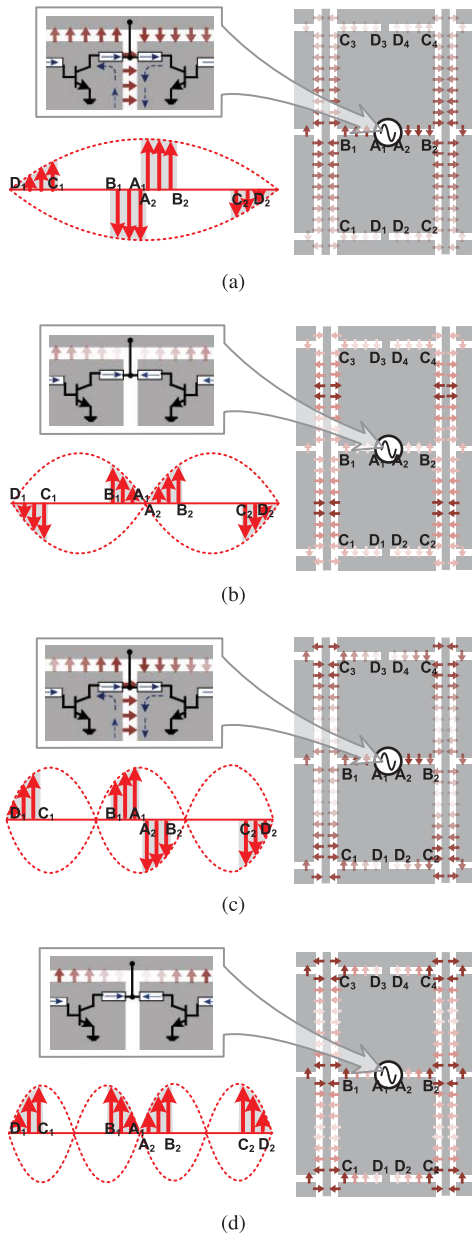


Fig. 12. Theoretical electrical-field distributions in branched resonator at different harmonics. (a) f_0 . (b) $2f_0$. (c) $3f_0$. (d) $4f_0$. Darker arrow color means higher field intensity.

$(\overline{D_3C_3}, \overline{D_4C_4})$, the standing wave formed inside one slotline is a 180° -rotated (out-of-phase) replica of that inside the other slotline. Therefore, radiation at f_0 from all horizontal slotlines in an element is canceled.

At $2f_0$ [see Fig. 12(b)], the waves injected into the left and right branched resonators are in-phase. We denote it as the *even* mode of the resonator pair. In contrast with the odd mode, in the even mode, standing waves inside each of the following slotline pairs— $(\overline{A_1B_1}, \overline{A_2B_2})$, $(\overline{D_1C_1}, \overline{D_2C_2})$, and $(\overline{D_3C_3}, \overline{D_4C_4})$ —are in-phase. As a result, the undesired radiation is not canceled within each horizontal slotline pairs. On the other hand, however, thanks to the *folded geometry* of the resonators, *vertically flipped* replica pairs of standing waves are formed in the following slotline

pairs: $(\overline{A_1B_1}, \overline{D_1C_1})$, $(\overline{A_1B_1}, \overline{D_3C_3})$, $(\overline{A_2B_2}, \overline{D_2C_2})$, and $(\overline{A_2B_2}, \overline{D_4C_4})$. Therefore, the radiation from $(\overline{A_1B_1}, \overline{A_2B_2})$ is canceled by the top half $(\overline{D_1C_1}, \overline{D_2C_2})$ and the bottom half of $(\overline{D_3C_3}, \overline{D_4C_4})$. By “half,” we mean that, each $\overline{D_iC_i}$ ($i = 1, 2, 3, 4$) slotline on the boundary is shared by two elements, so on average half of its radiation is contributed to each element⁸. In summary, the far-field radiation in all horizontal slotlines is canceled.

The case at $3f_0$ [see Fig. 12(c)] resembles that at f_0 : an odd mode is excited, and radiations in all horizontal slotlines are canceled.

At $4f_0$ [see Fig. 12(d)], an even mode is excited, and similar to the case at $2f_0$, the slotline pairs $(\overline{A_1B_1}, \overline{A_2B_2})$, $(\overline{D_1C_1}, \overline{D_2C_2})$, and $(\overline{D_3C_3}, \overline{D_4C_4})$ are radiative in their own right. However, there is a critical difference between the $4f_0$ case and the $2f_0$ case: because of the *phase inversion* at each midpoint of $\overline{B_iC_i}$ ($i = 1, 2, 3, 4$), standing waves formed in all the horizontal slotline pairs— $(\overline{A_1B_1}, \overline{A_2B_2})$, $(\overline{D_1C_1}, \overline{D_2C_2})$ and $(\overline{D_3C_3}, \overline{D_4C_4})$ —are *in-phase*. Therefore, in the far field, the radiation from $(\overline{A_1B_1}, \overline{A_2B_2})$ interferes constructively with the radiation from the top half of $(\overline{D_1C_1}, \overline{D_2C_2})$ and the bottom half of $(\overline{D_3C_3}, \overline{D_4C_4})$. In other words, there are on average two coherent dipole slot antennas at $4f_0$ in each element. We note again that inside the array of these elements, the horizontal and vertical spacing of all these antennas is the optimal value of $\lambda_{4f_0}/2$.

Fig. 13 shows the simulated electrical-field distributions in the branched resonator slots at different harmonics, which agree with those in Fig. 12. In the structure for EM simulation and the actual layout, on the upper metal plate of the element, there is a “dummy” triangular opening with the same shape as its lower counterpart. Its existence leads to a more symmetric field distribution. Fig. 14 shows the simulated antenna patterns and gains of one element and a 6×7 array at different harmonics. We see that only at $4f_0$ are the element and array radiative. Due to the presence of the silicon substrate, the radiation propagates toward the back side of the chip. In the simulation, a semi-infinite high-resistivity silicon medium is applied at the chip back, which is emulated by a hemispheric silicon lens in reality. The simulated radiation directivity and efficiency of the array at $4f_0$ are 23.6 dBi and 63%, respectively. The simulated frequency response of one antenna is given in Fig. 15.

D. Routing of DC Biases

Each oscillator pair requires the following dc biases: V_{CC} , V_B , and V_{EE} for the collectors, bases, and emitters of the transistors. Since the base current I_B is only 0.3 mA per element, Metal 1, which is $6 \mu\text{m}$ below Top-Metal 1, is used for V_B . In contrast, the collector current I_C is ~ 14 mA per element, the top-metal layers, with much larger maximum allowed current density, are used to feed V_{CC} and V_{EE} [see Fig. 4(b)]. Inside each element, slotline pair $(\overline{A_1B_1}, \overline{A_2B_2})$ divides the Top-Metal 1 plane into two dc-isolated halves:

⁸Alternatively, the radiation cancellation can also be considered to be only between $(\overline{A_1B_1}, \overline{A_2B_2})$ and $(\overline{D_1C_1}, \overline{D_2C_2})$, as shown in Fig. 12(b). The radiation from $(\overline{D_3C_3}, \overline{D_4C_4})$ is then canceled by the element above the current one.

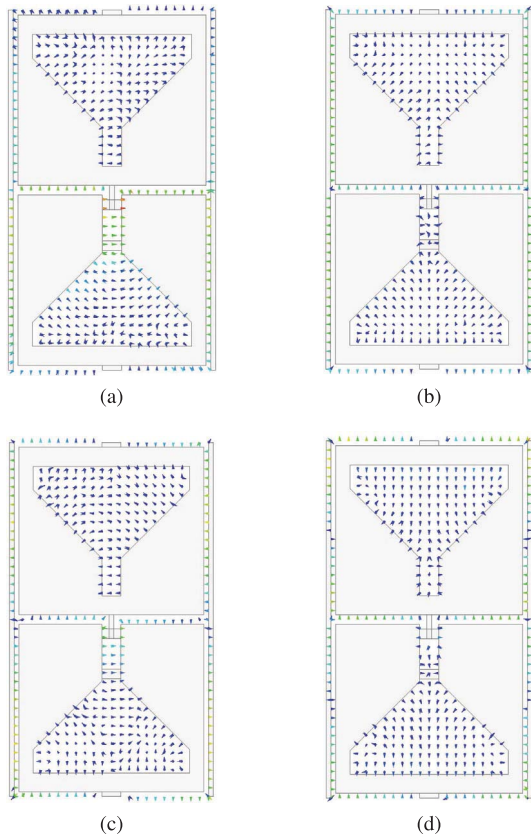


Fig. 13. HFSS simulation of magnitude and phase of electrical-field vectors in the slots at different harmonics. (a) f_0 . (b) $2f_0$. (c) $3f_0$. (d) $4f_0$. Input power at all frequencies is normalized to be the same.

the upper half is dc-connected to V_{CC} and the lower half is connected to V_{EE} . At the left/right boundary of the element, a metal bridge using Top-Metal 2 connects the metal plates so that the relevant dc power supply is fed horizontally. Last, it is also noteworthy that, on the boundary of two vertically adjacent elements, an ac short circuit for the branched resonator [see Fig. 12] is needed. To avoid directly connecting the V_{CC} plate of one element with the V_{EE} plate of the other, we use two 300-fF MIM capacitors to provide the ac short, as shown in Fig. 16. The self-resonance frequency of the MIM capacitor simulated by HFSS is 416 GHz. Beyond the self-resonance frequency, the capacitor impedance remains low ($\sim 2.3 \Omega$ at 1 THz) and serves as a good ac short.

E. Boundaries of the Array

The radiator elements at the array boundaries are lack of horizontally and/or vertically adjacent counterparts. Therefore, proper boundary conditions should be provided so as to confine the oscillation and harmonic waves within the array. As described in Section IV-A, for the horizontal boundaries of the elements, an electrical-short condition (i.e., electrical field is perpendicular to the boundary) is required; for the vertical boundaries of the elements, an electrical-open condition (i.e., electrical field is in parallel with the boundary) is required.

To provide the electrical-short condition at the top/bottom boundaries, a thick metal “wall” implemented by a Metal 1 to

Top-Metal 2 stack is used, so that all electrical-field vectors are perpendicularly terminated at the metal wall.

At the left/right boundaries, dc power supplies should be provided from two columns of pads, but potential signal leakage at f_0 and $4f_0$ through these paths should be prevented, so that the oscillation and radiation are not affected. To this end, a notch filter connected to each boundary metal bridge is designed. Fig. 17 shows the structure of the filters and other neighboring components at the array boundary. All filters are identical, and they present high impedances near f_0 and $4f_0$. Each is implemented by three sections of microstrip lines: \overline{AB} , \overline{DB} , and \overline{CB} , of which the lengths are $(1/2)\lambda_{4f_0}$, $(1/4)\lambda_{4f_0}$, and $(1/4)\lambda_{4f_0}$, respectively. Node A is short-circuit terminated, whereas Node D is open-circuit terminated. It can be inferred from the Smith chart in Fig. 18(a) that at both f_0 and $4f_0$ impedances presented at Node C are high. The simulated impedances are shown in Fig. 18(b).

V. CHIP PROTOTYPE AND EXPERIMENTAL RESULTS

The chip is fabricated in the IHP 130-nm SiGe BiCMOS process featuring an HBT f_{max} of 450 GHz [30]. There are in total 6×7 elements and 91 dipole slot antennas⁹ on the $1 \times 1 \text{ mm}^2$ chip area. The micrographs of the chip and a single element are shown in Fig. 19(a). A hemispheric, high-resistivity silicon lens is attached on the chip back for the radiation coupling to the free space, as shown in Fig. 19(b). The dimensions of the wafer between silicon lens and the chip substrate are $2 \text{ cm} \times 2 \text{ cm} \times 500 \mu\text{m}$, and the resistivity is $20 \text{ k}\Omega \cdot \text{cm}$. We found that when the dimension of the inserted wafer is much larger than the diameter of the silicon lens ($D_{lens} = 1 \text{ cm}$), the radiation efficiency is nearly not affected. The dc power consumption when the chip reaches the maximum output power is $P_{dc} = V_{CC} \cdot I_C + V_B \cdot I_B = 1.8 \text{ V} \times 0.6 \text{ A} + 1.15 \text{ V} \times 12 \text{ mA} = 1.1 \text{ W}$.

A. Measurement of the Oscillation/Output Frequencies

Previously, the spectrum in the mid-THz range was measured using a Fourier transform infrared spectrometer [9]. Some sub-harmonic mixers [31] are able to detect 1-THz signal. However, they require high-power LO signal with frequency beyond 300 GHz.

Due to the inaccessibility of a heterodyne receiver to directly down-convert the 1-THz signal for frequency measurement, we use an indirect approach, which is based on the down-conversion of the leaked radiation at the fundamental frequency to measure f_0 ; the output frequency of $4f_0$ can then be inferred. In our simulation, the total oscillation power that the transistors generate at f_0 (flowing from collectors to bases) is as high as 400 mW. Device mismatch across the array (hence imperfect radiation cancellation) should then cause detectable signal leakage at f_0 . Fig. 20 shows the measurement setup. The radiation leakage is received by a WR-3.4 diagonal horn antenna placed near the silicon lens and is then fed into a 16th-harmonic WR-3.4 mixer from Virginia Diode Inc. (VDI). Meanwhile, a 10-dBm LO signal at

⁹The radiator elements on the top and bottom of the array do not share antennas. The total number of antennas is, therefore, $6 \times 7 \times 2 + 7 = 91$.

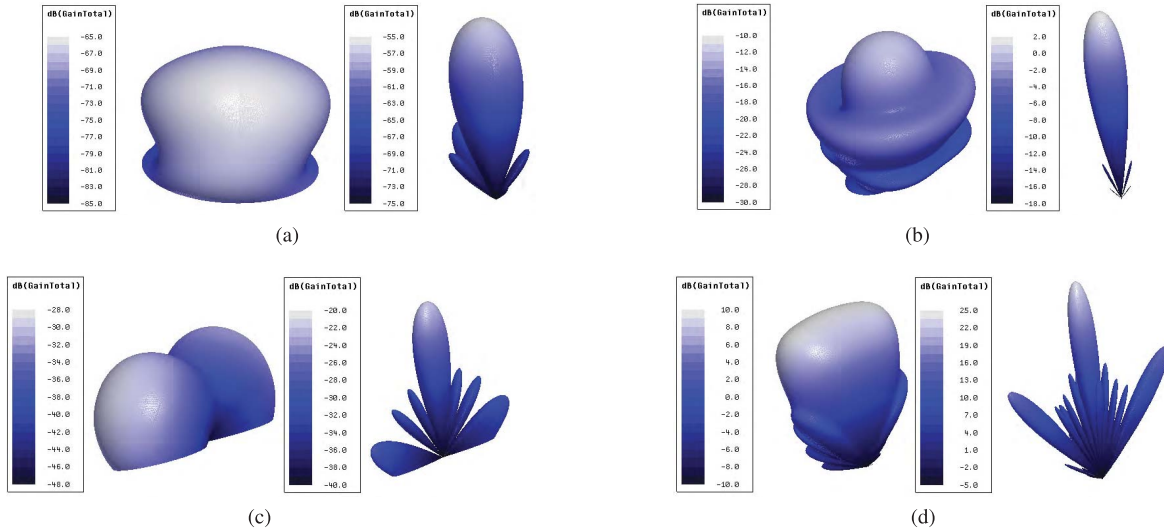


Fig. 14. HFSS simulation of antenna gain at (a) f_0 , (b) $2f_0$, (c) $3f_0$, and (d) $4f_0$ ($f_0 = 250$ GHz) of a single element (left) and a 6×7 array (right). Note that the antenna gain at $4f_0$ is 20~75 dB higher than that in the other cases. At f_0 and $2f_0$, antenna gain increases by only ~ 10 dB from single element to array due to the close spacing (relative to wavelength) between antennas. At $3f_0$, antenna gain increases by only ~ 8 dB, because the peak gain of single element is not in the perpendicular direction. At $4f_0$, there is ~ 15 dB gain increase, which matches the theoretical prediction: $10 \log_{10}(42) = 16$ dB.

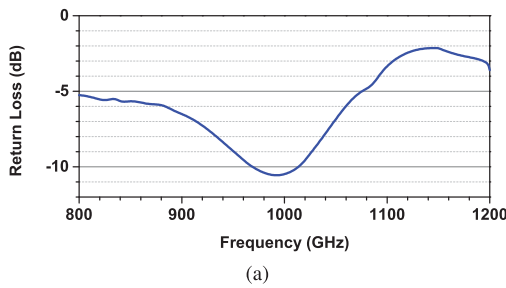


Fig. 15. Simulated return loss of the dipole slot antenna in a single element with even-mode excitation.

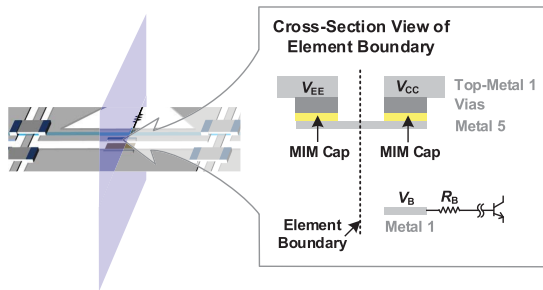


Fig. 16. AC-coupling structure using two MIM capacitors.

around 15.8 GHz is applied. The output IF spectrum from the even-harmonic mixer (EHM), amplified by an amplifier chain and measured by a spectrum analyzer, is shown in Fig. 21(a). Only one peak is obtained, indicating that the fundamental oscillations of all elements are synchronized. The value of oscillation frequency f_0 can be calculated as

$$f_0 = 16f_{LO} \pm f_{IF} \quad (9)$$

where the factor of 16 is verified by slightly increasing f_{LO} and measuring the resultant change of f_{IF} ($|\Delta f_{IF}| = 16|\Delta f_{LO}|$). The sign of “ \pm ” is the opposite of that of $|\Delta f_{LO}|$.

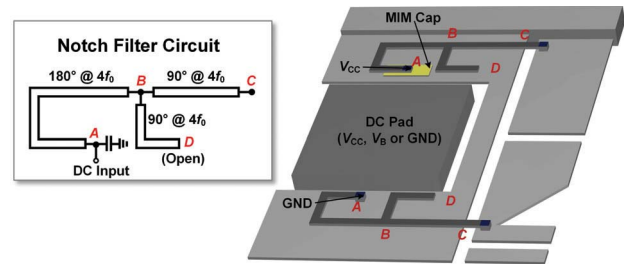


Fig. 17. Structure of the top-left boundary of the entire array, including the notch filters. The structure is repeated for each row, except that the dc pads are connected to different biases.

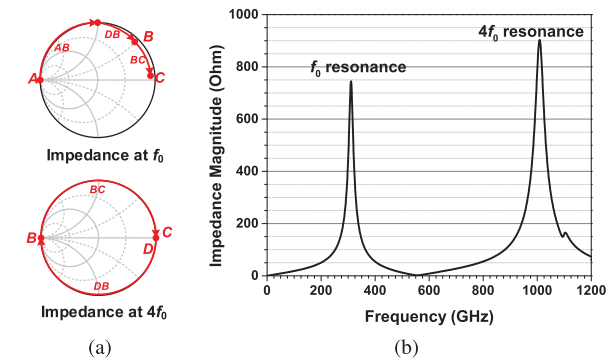


Fig. 18. (a) Synthesis of high impedances at f_0 and $4f_0$ using the notch filter at array boundaries. (b) Simulated magnitude of the filter impedances.

According to (9), the fundamental oscillation frequencies at various HBT base bias voltages V_B are shown in Fig. 21(b). When increasing V_B from 1.05 to 1.2 V, f_0 decreases from 254 to 252.8 GHz (due to larger C_{π} of each HBT). The actual tuning range may be larger than this, but it is not characterized due to the small SNR in Fig. 21(a). The degradation of the received power when base bias is too high or too low is mainly

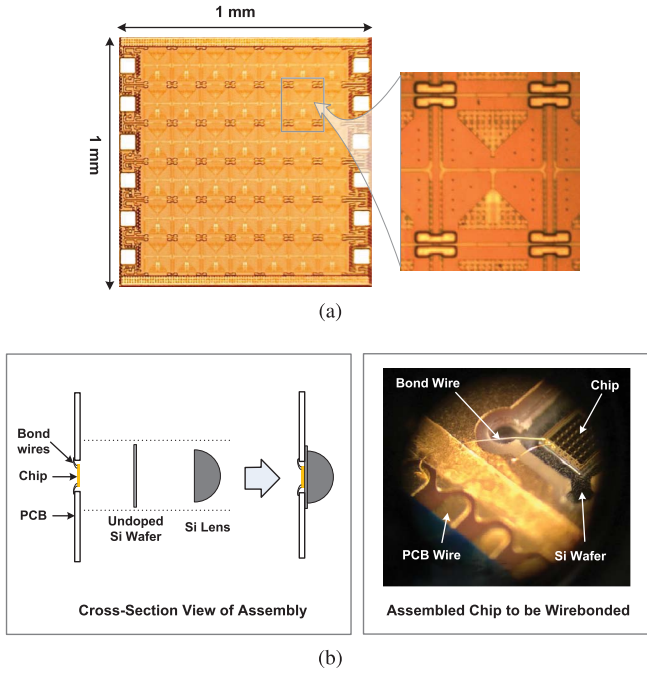


Fig. 19. (a) Die photograph of the chip and a zoomed-in image of a single element. (b) Diagram and photograph of the chip assembly for backside radiation.

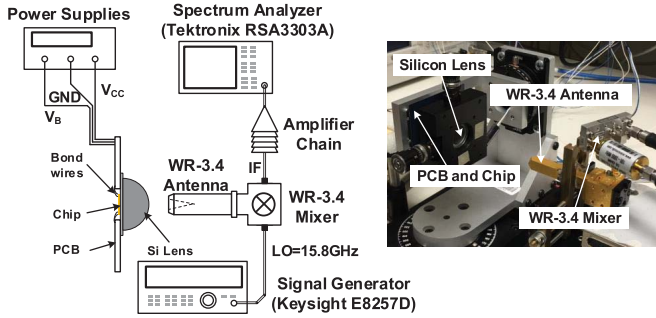


Fig. 20. Setup of measuring fundamental frequency f_0 using an EHM.

due to a departure from the optimal oscillation condition and high- Q frequency response of the branched resonators. The values of f_0 for 5 chip samples are measured, which range from 249 to 254 GHz at the optimum bias point, showing small process variation.

The output radiation at $4f_0$ should then change from 1011.2 to 1016 GHz. Last, Fig. 21(b) also shows the measured IF power (normalized) at various V_B , which we use to evaluate the oscillation activity. It peaks at $V_B = 1.15$ V, corresponding to $f_0 = 253.2$ GHz ($4f_0 = 1.013$ THz).

B. Characterizations of the 1-THz Radiation

The total radiated power of the 1-THz signal is measured using a WR-1.0 diagonal antenna (directivity = 25 dBi) cascaded with a VDI WR-1.0 zero-bias diode (ZBD) detector. The detector has a calibrated responsivity of 1.1 kV/W and an noise-equivalent power of 57 pW/ $\sqrt{\text{Hz}}$ at 1 THz (calibration data specific to individual product are provided by VDI). The testing setup is shown in Fig. 22. The chip and the diagonal

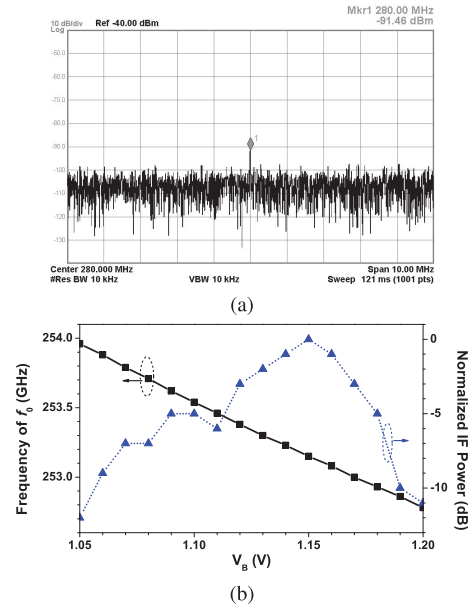


Fig. 21. Measurement results of the leaked radiation at f_0 . (a) IF spectrum down-converted by an EHM. (b) Frequency and relative power at different V_B biases.

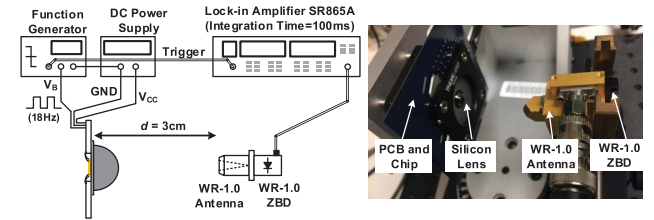


Fig. 22. Setup for the 1-THz radiation pattern and power measurements using a WR-1.0 ZBD detector. Note that the lock-in amplifier measures the root-mean-square voltage of the fundamental sinusoidal component of the detector output signal; therefore, an additional multiplication factor of $\pi/\sqrt{2}$ (or 2.22 times) is used [32] when calculating the peak-to-peak voltage of the output square wave (hence the radiated power).

antenna are separated with a distance of 3 cm. According to the result presented in Fig. 23, 3 cm is already in the far-field range. First, the radiation is electronically modulated by connecting V_B of the chip to an 18-Hz square wave with 50% duty cycle and 1.15-V peak voltage. This is to facilitate the lock-in amplifier for narrow-band noise suppression and to ensure that the slow-varying heat radiation is not included in the measured power result. From the reading of the lock-in amplifier, the power received by the ZBD P_{RX} is calculated to be 4 μ W. Using the Friis equation [17]

$$\text{EIRP} = P_{TX} \cdot D_{TX} = P_{RX} \cdot \left(\frac{4\pi d}{\lambda}\right)^2 / D_{RX} \quad (10)$$

where $D_{RX} = 25$ dBi, $d = 3$ cm, and $\lambda = 300$ μ m, and the EIRP of the chip is determined to be 13.1 dBm (or 20.4 mW).

Next, the chip is rotated with different azimuthal (θ) and polar (φ) angles. Fig. 24 shows the measured and simulated 1-THz radiation patterns in the E -plane and H -plane, respectively. Note that our array is a planar array with narrow radiation beam, which enables the calculation of the peak

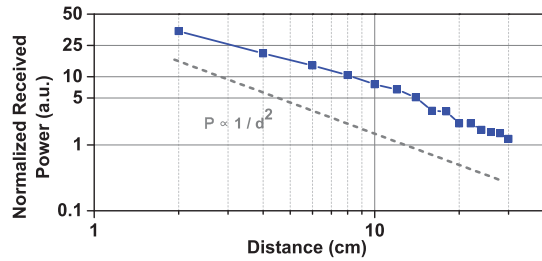


Fig. 23. Measured received power of the 1-THz signal at varying distance.

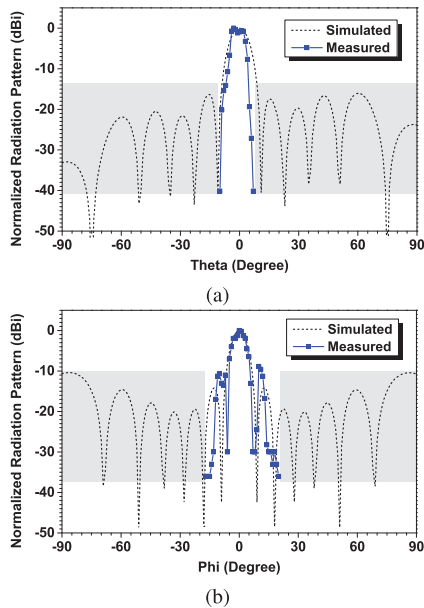


Fig. 24. Measured radiation pattern of 1-THz signal. (a) E -plane. (b) H -plane. Shaded regions represent the angular range where the measured response is below noise floor, which could be due to the blocking of radiation by the metal fixture for the silicon lens.

directivity using the following equation [33]:

$$D_0 = \frac{32400}{\theta_h \cdot \varphi_h}. \quad (11)$$

Here, θ_h and φ_h (in degrees) are half-power beamwidth in the E -plane and H -plane, respectively. For our case, $\theta_h = 11^\circ$ and $\varphi_h = 11^\circ$, and thus, we have $D_0 = 24$ dBi. This, along with the aforementioned 13.1 dBm of measured EIRP, gives an integrated radiation power (over the measurable angle range in Fig. 24) of -10.9 dBm (or $80 \mu\text{W}$). According to the comparison between the simulated and measured radiation patterns in Fig. 24, some sidelobes are not measured due to the blocking of radiations by the silicon lens fixture. Therefore, the actual total radiated power is higher than $80 \mu\text{W}$, although the discrepancy should be small due to the low intensity of these unmeasured sidelobes.

Notably, the supported frequency band of the WR-1.0 waveguide used in our setup ranges from 750 to 1100 GHz. As a result, any leakage at 253 and 506 GHz is completely excluded from our power measurement results. Although the third-harmonic leakage at 759 GHz cannot be filtered out by the waveguide, we believe its impact is negligible, because the differential field distribution at $3f_0$ should suppress the

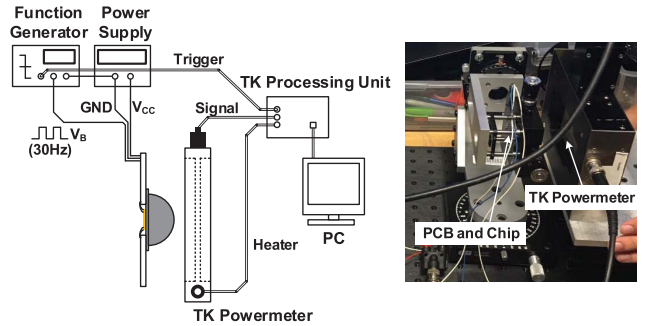


Fig. 25. Setup of measuring total radiated RF power using TK photo-acoustic power meter.

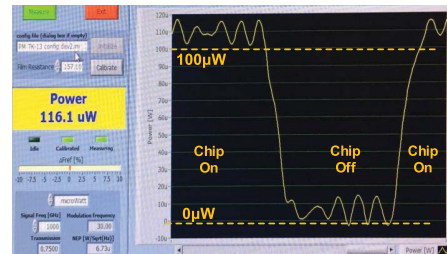


Fig. 26. Measured total radiated RF power when chip is power ON, then power OFF, and finally power ON again.

leakage by $10 - (-28) = 38$ dB (see Fig. 14), compared with the radiation at $4f_0$. This is also verified by the good consistency between the simulated and measured radiation patterns in Fig. 24.

Last, the total radiated power is also measured using a photo-acoustic Thomas Keating (TK) absolute power meter (see Fig. 25), which has a large input window to capture radiation from most of the directions including sidelobes (although the majority of the received power is still attributed to the main lobe). Similar to the setup in Fig. 22, the power meter also uses a lock-in function to minimize the impact of the thermal radiation. The measured results are shown in Fig. 26. During the time period presented here, the SiGe chip is first turned *on* (i.e., V_B is connected to a 30-Hz 50% duty cycle $1.15V_{pp}$ square wave), then *off* (i.e., V_B is grounded), and finally *on* again. The measured radiated power is $\sim 100 \mu\text{W}$ (-10 dBm). The 0.9-dB difference between that and the radiated power measured by the ZBD is believed to be caused by the leaked radiation at f_0 , as well as the limited instrumental accuracy. The measurement results from the TK power meter mainly serve as a sanity check for the ZBD measurement. With a grating filter centered at 1 THz, more accurate power value may be obtained from the TK power meter.

VI. CONCLUSION

This paper presents a scalable array architecture suitable for generating coherent high-power radiation in the mid-THz band. The highlight of the work is a multi-functional branched resonator structure in each element, ensuring structural compactness and high efficiency which are necessary for this band. A chip prototype has proven that the architecture is able to integrate at least 42 oscillators and 91 antennas, which

TABLE I
 COMPARISON OF MID-THZ COHERENT RADIATORS IN SILICON

	This Work	[6]	[7]	[10]	[9]	[8]	[11]
Circuit Type	Oscillator	Active Multiplier			Passive Multiplier		Pulse Generator
f_{out} (THz)	1.01	0.99	0.82	0.92	1.33	0.73	1.1
P_{out} (dBm)	-10.9	-37	-29	-17.3	-22.7	-21.3	N/A
EIRP (dBm)	13.1	N/A	-17	-10	-13	-22.2	-70
$P_{\text{RF,in}}$ (dBm)	Not Needed	8	14	8	18	13.8	Not Needed
P_{DC} (W)*	1.1	4	3.7	5.7×10^{-3}	0	0	0.105
DC-to-RF Efficiency *	0.73×10^{-4}	0.5×10^{-7}	3.4×10^{-7}	3.3×10^{-2}	N/A	N/A	N/A
Number of Antennas	91	4	4	2	2	1	1
Method of Array Sync.	2D Slotline Coupling	Input RF Power Splitting		Output RF Power Splitting		N/A	N/A
Area (mm ²)	1.0	3.28	3.22	0.37	0.36	0.26	0.47
Technology	130-nm SiGe	250-nm SiGe	250-nm SiGe	130-nm SiGe	65-nm CMOS	65-nm CMOS	130-nm SiGe

* Most THz multipliers require a large-power, sub-THz driving signal, and the power consumption associated with the generation of such signal is not included here. In comparison, this work is self-sustaining and requires no input signal.

coherently radiate $80 \mu\text{W}$ of 1-THz signal with a high directivity of 24 dBi. The measured chip performance is compared with other mid-THz coherent radiators in silicon in Table I. To the best of our knowledge, the chip has demonstrated the highest total radiated power and highest EIRP among all radiators at above 0.6 THz.

Since this array technology mainly lies at the EM level, it is also applicable for other solid-state devices with higher speed/power performance, such as InP HBT/HEMT and GaN HEMT. Output power level at 1 mW and above should be feasible.

APPENDIX

PHASE MISMATCH IN COUPLED OSCILLATORS

In our analysis for the coupled system shown in Fig. 10(a), each free-running self-feeding oscillator is modeled as an oscillating parallel RLC tank sustained by a negative resistance provided by transistors [see Fig. 27(a)]: $-R_{\text{tank},1} \approx -R_{\text{tank},2} = -R_{\text{tank}}$. The coupled two-oscillator system, at steady state, can be decomposed into a common-mode component, which is the desired mode, and a differential-mode component, which is a result of the oscillation frequency mismatch $\Delta\omega$ and the cause for injection current in each oscillator. Accordingly, following the expressions of the oscillator voltages $v_1(t)$ and $v_2(t)$ given in (5), we define their common-mode voltage v_0 as:

$$\begin{aligned} v_0 &= \frac{v_1 + v_2}{2} = e^{j\omega_0 t} \cdot (A_0 \cos \Delta\theta + j \Delta A \sin \Delta\theta) \\ &\approx A_0 \cos \Delta\theta \cdot e^{j\omega_0 t} \end{aligned} \quad (12)$$

and differential-mode voltage Δv as

$$\begin{aligned} \Delta v &= \frac{v_1 - v_2}{2} = e^{j\omega_0 t} \cdot (\Delta A \cos \Delta\theta + j A_0 \sin \Delta\theta) \\ &= A_0 \sin \Delta\theta \sqrt{1 + \left(\frac{\Delta A}{A_0 \tan \Delta\theta}\right)^2} \cdot e^{j(\omega_0 t + \arctan(\frac{A_0 \tan \Delta\theta}{\Delta A}))}. \end{aligned} \quad (13)$$

Next, we note that the coupled network in Fig. 10(a) resembles a Wheatstone bridge, and has the following properties.

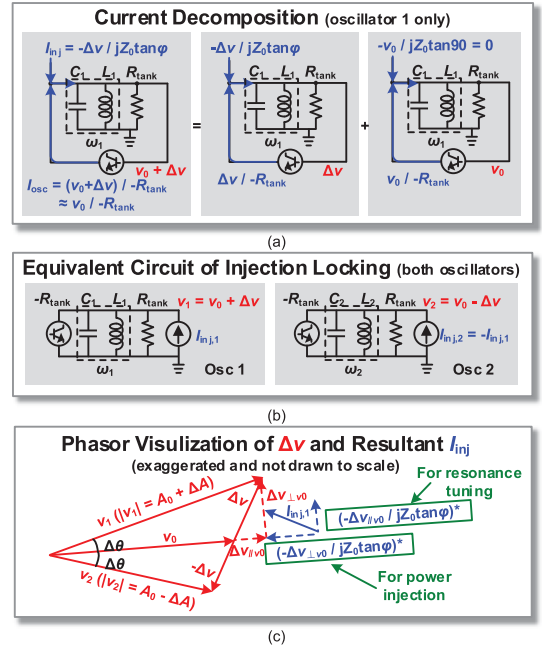


Fig. 27. Graphical explanation of the current injection caused by Δv .

- 1) For v_0 in each oscillator, the short connection at φ of the transmission lines is “invisible,” and thus, this mode only shows a $\pi/2$ -long resonator pair.
- 2) For $\pm\Delta v$ in each oscillator, the short connection at φ of the lines is “visible” and a virtual ground is formed there.

Hence, the main oscillation current of each oscillator is

$$i_{\text{osc},i} = (v_0 \pm \Delta v) / R_{\text{tank}} \approx v_0 / R_{\text{tank}} \quad (i = 1, 2) \quad (14)$$

and the injected current for each oscillator is

$$i_{\text{inj},i} = \mp \Delta v / (jZ_0 \tan \varphi) \quad (i = 1, 2). \quad (15)$$

These definitions are consistent with Adler’s model in [23] and [34]. Also, suppose the loss of the branched resonator is

low [see Fig. 7(a)], we show in Fig. 27(a) the current decomposition details of Oscillator 1. (For Oscillator 2, the only difference is that current is injected in the reverse direction.)

Next, we derive the relationship between $\Delta\theta$ and ΔA . This can be done by using energy conservation. The power injected into Oscillator 1 is

$$\begin{aligned} P_{\text{inj},1} &= \frac{1}{2} \text{Re} \left((v_0 + \Delta v) \cdot \left(\frac{-\Delta v}{jZ_0 \tan \varphi} \right)^* \right) \\ &= \frac{\text{Im}(v_0 \Delta v^*)}{2Z_0 \tan \varphi} \approx \frac{A_0^2 \cos \Delta\theta \sin \Delta\theta}{2Z_0 \tan \varphi}. \end{aligned} \quad (16)$$

For the time being, we assume $\Delta\theta > 0$; then, (16) is positive, meaning that Oscillator 1 receives power from Oscillator 2 via the two connected transmission-line stubs. By comparing (12) and (13), we see that the imaginary part of Δv is perpendicular to v_0 , which is $\Delta v_{\perp v_0} = jA_0 \sin \Delta\theta \cdot e^{j\omega_0 t}$. Substituting this part into (15), a current in-phase with v_0 is generated, which is the cause of the positive power flow injected into Oscillator 1. A qualitative phasor diagram is given in Fig. 27(c).

Next, since the real part of Δv is in parallel with the v_0 vector and is expressed as $\Delta v_{\parallel v_0} = \Delta A \cos \Delta\theta \cdot e^{j\omega_0 t}$, the extra power of Oscillator 1, $\Delta P_{\text{osc},1}$, presented on R_{tank} is

$$\Delta P_{\text{osc},1} = \frac{||v_0 + \Delta v_{\parallel v_0}||^2 - ||v_0||^2}{2R_{\text{tank}}} \approx \frac{A_0 \Delta A \cos \Delta\theta}{R_{\text{tank}}} \quad (17)$$

which is the result of the injection through coupling, so

$$\Delta P_{\text{osc},1} = P_{\text{inj},1}. \quad (18)$$

Use (16)–(18) and let $k(\varphi) = ((R_{\text{tank}})/(Z_0 \tan \varphi))$, then we have

$$\sin \Delta\theta \approx \tan \Delta\theta = \frac{2Z_0 \tan \varphi}{R_{\text{tank}}} \cdot \frac{\Delta A}{A_0} = k(\varphi)^{-1} \cdot \frac{\Delta A}{A_0} \quad (19)$$

which can be then substituted into (13) and give

$$\begin{aligned} \Delta v &= A_0 \sin \Delta\theta \sqrt{1 + k(\varphi)^2} \cdot e^{j(\omega_0 t + \arctan(k(\varphi)^{-1}))} \\ &\approx A_0 k(\varphi) \sin \Delta\theta \cdot e^{j(j\omega_0 t + jk(\varphi)^{-1})}. \end{aligned} \quad (20)$$

Note that $k(\varphi) \gg 1$, i.e., $R_{\text{tank}} \gg Z_0 \tan \varphi$, is used in the above approximation.¹⁰ Finally, we apply Adler's equation in the case of modulated sinusoid injection [34], i.e.,

$$\frac{d\theta_{\text{osc}}}{dt} = \omega_i - \omega_0 - \frac{\omega_i}{2Q} \cdot \frac{|i_{\text{inj}}|}{|i_{\text{osc}}|} \cdot \sin(\theta_{\text{osc}} - \theta_{\text{inj}}) \quad (21)$$

where ω_i is the resonance frequency of the tank of Oscillator 1 or 2. Using (12), (14), (15), and (20), we have $|i_{\text{inj},i}|/|i_{\text{osc},i}| \approx k(\varphi)^2 \cdot \tan \Delta\theta$, $\theta_{\text{osc}} = \angle v_0 = (\Delta A/A_0) \cdot \tan \Delta\theta \approx 0$, $\theta_{\text{inj},1} = k(\varphi)^{-1} + \pi/2 \approx \pi/2$, and $\theta_{\text{inj},2} = k(\varphi)^{-1} - \pi/2 \approx -\pi/2$. Therefore, we have the following equations for Oscillators 1 and 2:

$$0 = \omega_1 - \omega_0 - \frac{\omega_1}{2Q} \cdot k(\varphi)^2 \tan \Delta\theta \cdot \sin(0 + \pi/2) \quad (22)$$

$$0 = \omega_2 - \omega_0 - \frac{\omega_2}{2Q} \cdot k(\varphi)^2 \tan \Delta\theta \cdot \sin(0 - \pi/2). \quad (23)$$

¹⁰As a side note, $k(\varphi) \gg 1$ also indicates that the amount of injected current used to tune frequency is much larger than that for power injection.

Adding (22) and (23), we get

$$\omega_0 = \frac{\omega_1 + \omega_2}{2} - \frac{\omega_1 - \omega_2}{2Q} \cdot k(\varphi)^2 \tan \Delta\theta \approx \frac{\omega_1 + \omega_2}{2} \quad (24)$$

with the approximation that

$$\omega_1 \gg \frac{\Delta\omega}{Q} \cdot k(\varphi)^2 \tan \Delta\theta \Leftrightarrow \frac{\Delta\omega \cdot L_1}{Z_0 \tan \varphi} \cdot \frac{\Delta A}{A_0} \ll 1 \quad (25)$$

which is readily satisfied. Meanwhile, by subtracting (23) from (22) and using $\omega_1 + \omega_2 \approx 2\omega_0$, we have

$$\omega_1 - \omega_2 = \frac{\omega_0}{Q} \cdot k(\varphi)^2 \tan \Delta\theta \quad (26)$$

which gives the phase difference between $v_1(t)$ and $v_2(t)$

$$2\Delta\theta = 2 \arctan \left(\frac{\omega_1 - \omega_2}{\omega_0} \cdot Q \cdot \frac{Z_0^2 \tan^2 \varphi}{R_{\text{tank}}^2} \right). \quad (27)$$

ACKNOWLEDGMENT

The authors would like to thank C. Wang and Prof. Q. Hu's group at MIT for chip testing assistance. The chip fabrication was supported by IHP Microelectronics.

REFERENCES

- [1] R. Al Hadi *et al.*, "A 1 k-pixel video camera for 0.7–1.1 terahertz imaging applications in 65-nm CMOS," *IEEE J. Solid-State Circuits*, vol. 47, no. 12, pp. 2999–3012, Dec. 2012.
- [2] T. Globus *et al.*, "Sub-terahertz vibrational spectroscopy for microRNA based diagnostic of ovarian cancer," *Convergent Sci. Phys. Oncol.*, vol. 2, no. 4, p. 045001, Oct. 2016.
- [3] M. M. Assefzadeh *et al.*, "Terahertz trace gas spectroscopy based on a fully-electronic frequency-comb radiating array in silicon," in *Proc. CLEO, Sci. Innov.*, Washington, DC, USA, Jun. 2016, pp. 7–8.
- [4] C. Wang and R. Han, "Rapid and energy-efficient molecular sensing using dual mm-Wave combs in 65 nm CMOS: A 220-to-320 GHz spectrometer with 5.2 mW radiated power and 14.6-to-19.5 dB noise figure," in *IEEE Int. Solid-State Circuits Conf. (ISSCC) Dig. Tech. Papers*, vol. 60. San Francisco, CA, USA, Feb. 2017, pp. 302–303.
- [5] J. C. Chen and S. Kaushik, "Terahertz interferometer that senses vibrations behind barriers," *IEEE Photon. Technol. Lett.*, vol. 19, no. 7, pp. 486–488, Apr. 1, 2007.
- [6] K. Statnikov, J. Grzyb, B. Heinemann, and U. R. Pfeiffer, "160-GHz to 1-THz multi-color active imaging with a lens-coupled SiGe HBT chipset," *IEEE Trans. Microw. Theory Techn.*, vol. 63, no. 2, pp. 520–532, Feb. 2015.
- [7] E. Öjefors, J. Grzyb, Y. Zhao, B. Heinemann, B. Tillack, and U. R. Pfeiffer, "A 820 GHz SiGe chipset for terahertz active imaging applications," in *IEEE Int. Solid-State Circuits Conf. (ISSCC) Dig. Tech. Papers*, San Francisco, CA, USA, Feb. 2011, pp. 224–225.
- [8] Z. Ahmad and K. K. O, "0.65–0.73 THz quintupler with an on-chip antenna in 65-nm CMOS," in *IEEE Symp. VLSI Circuits, Dig. Tech. Papers*, Kyoto, Japan, Jun. 2015, pp. C310–C311.
- [9] Z. Ahmad, M. Lee, and K. K. O, "1.4 THz, –13 dBm-EIRP frequency multiplier chain using symmetric- and asymmetric-CV varactors in 65 nm CMOS," in *IEEE Int. Solid-State Circuits Conf. (ISSCC) Dig. Tech. Papers*, vol. 59. San Francisco, CA, USA, Jan./Feb. 2016, pp. 350–351.
- [10] H. Aghasi, A. Cathelin, and E. Afshari, "A 0.92-THz SiGe power radiator based on a nonlinear theory for harmonic generation," *IEEE J. Solid-State Circuits*, vol. 52, no. 2, pp. 406–422, Feb. 2017.
- [11] M. M. Assefzadeh and A. Babakhani, "Broadband oscillator-free THz pulse generation and radiation based on direct digital-to-impulse architecture," *IEEE J. Solid-State Circuits*, vol. 52, no. 11, pp. 2905–2919, Nov. 2017.
- [12] K. Sengupta and A. Hajimiri, "A 0.28 THz 4 × 4 power-generation and beam-steering array," in *IEEE Int. Solid-State Circuits Conf. (ISSCC) Dig. Tech. Papers*, vol. 55. San Francisco, CA, USA, Feb. 2012, pp. 256–257.

- [13] R. Han and E. Afshari, "A CMOS high-power broadband 260-GHz radiator array for spectroscopy," *IEEE J. Solid-State Circuits*, vol. 48, no. 12, pp. 3090–3104, Dec. 2013.
- [14] R. Han *et al.*, "A SiGe terahertz heterodyne imaging transmitter with 3.3 mW radiated power and fully-integrated phase-locked loop," *IEEE J. Solid-State Circuits*, vol. 50, no. 12, pp. 2935–2947, Dec. 2015.
- [15] U. R. Pfeiffer *et al.*, "A 0.53 THz reconfigurable source module with up to 1 mW radiated power for diffuse illumination in terahertz imaging applications," *IEEE J. Solid-State Circuits*, vol. 49, no. 12, pp. 2938–2950, Dec. 2014.
- [16] Y. Tousei and E. Afshari, "A high-power and scalable 2-D phased array for terahertz CMOS integrated systems," *IEEE J. Solid-State Circuits*, vol. 50, no. 2, pp. 597–609, Feb. 2015.
- [17] R. L. Haupt, *Antenna Arrays: A Computational Approach*. Hoboken, NJ, USA: Wiley, 2010.
- [18] C. Wang, Z. Hu, G. Zhang, J. Holloway, and R. Han, "Large-scale terahertz active arrays in silicon using highly-versatile electromagnetic structures," in *IEDM Tech. Dig.*, San Francisco, CA, USA, Dec. 2017, paper 12.3. [Online]. Available: <https://iee-iedm.org/session-12-circuit-and-device-interaction-circuit-device-challenges-in-more-moore-and-more-than-moore/>
- [19] S. Jameson, E. Halpern, and E. Socher, "A 300 GHz wirelessly locked 2×3 array radiating 5.4 dBm with 5.1% DC-to-RF efficiency in 65 nm CMOS," in *IEEE Int. Solid-State Circuits Conf. (ISSCC) Dig. Tech. Papers*, vol. 59. San Francisco, CA, USA, Jan./Feb. 2016, pp. 348–349.
- [20] B. A. Floyd, C.-M. Hung, and K. K. O, "Intra-chip wireless interconnect for clock distribution implemented with integrated antennas, receivers, and transmitters," *IEEE J. Solid-State Circuits*, vol. 37, no. 5, pp. 543–552, May 2002.
- [21] D. Dregely, R. Taubert, J. Dorfmueller, R. Vogelgesang, K. Kern, and H. Giessen, "3D optical Yagi-Uda nanoantenna array," *Nature Commun.*, vol. 2, p. 267, Apr. 2011.
- [22] R. L. Schmid, A. Ç. Ulusoy, S. Zeinolabedinzadeh, and J. D. Cressler, "A comparison of the degradation in RF performance due to device interconnects in advanced SiGe HBT and CMOS technologies," *IEEE Trans. Electron Devices*, vol. 62, no. 6, pp. 1803–1810, Jun. 2015.
- [23] B. Razavi, "A study of injection locking and pulling in oscillators," *IEEE J. Solid-State Circuits*, vol. 39, no. 9, pp. 1415–1424, Sep. 2004.
- [24] B. Razavi, *Design of Analog CMOS Integrated Circuits*. New York, NY, USA: McGraw-Hill, 2001.
- [25] Z. Hu and R. Han, "Fully-scalable 2D THz radiating array: A 42-element source in 130-nm SiGe with 80-μW total radiated power at 1.01 THz," in *IEEE Radio Freq. Integr. Circuits Symp. Dig. Papers*, Honolulu, HI, USA, Jun. 2017, pp. 372–375.
- [26] K. C. Gupta, R. Garg, I. Bahl, and P. Bhartia, *Microstrip Lines and Slotlines*. Norwood, MA, USA: Artech House, 1996. [Online]. Available: <http://us.artechhouse.com/Microstrip-Lines-and-Slotlines-3rd-Edition-P1579.aspx>
- [27] R. Spence, *Linear Active Networks*. Hoboken, NJ, USA: Wiley, 1970.
- [28] O. Momeni and E. Afshari, "High power terahertz and millimeter-wave oscillator design: A systematic approach," *IEEE J. Solid-State Circuits*, vol. 46, no. 3, pp. 583–597, Mar. 2011.
- [29] S. V. Robertson and L. P. B. Katehi, "A planar quasi-optical mixer using a folded-slot antenna," *IEEE Trans. Microw. Theory Techn.*, vol. 43, no. 4, pp. 896–898, Apr. 1995.
- [30] B. Heinemann *et al.*, "SiGe HBT technology with f_T/f_{\max} of 300 GHz/500 GHz and 2.0 ps CML gate delay," in *IEDM Tech. Dig.*, Dec. 2010, pp. 30.5.1–30.5.4.
- [31] Virginia Diodes Inc. *Product Catalog*. Accessed: Nov. 15, 2017. [Online]. Available: <https://vadiodes.com/en/products/spectrum-analyzer>
- [32] *Operational Manual of SR865A*, Stanford Res. Syst., Sunnyvale, CA, USA, 2014.
- [33] C. A. Balanis, *Antenna Theory: Analysis and Design*, 3rd ed. Hoboken, NJ, USA: Wiley, 2005.
- [34] B. Razavi, "Mutual injection pulling between oscillators," in *Proc. Custom Integr. Circuits Conf.*, Sep. 2006, pp. 675–678.



Zhi Hu (S'15) received the B.S. degree in microelectronics from Fudan University, Shanghai, China, in 2015. He is currently pursuing the Ph.D. degree at the Massachusetts Institute of Technology, Cambridge, MA, USA, with a focus on exploring novel architectures of terahertz circuits.

Mr. Hu received the SCSK Scholarship in 2013 and the KLA-Tencor Scholarship in 2014. He was a recipient of the Best Student Paper Award (second place) of the IEEE Radio-Frequency Integrated Circuits Symposium 2017.



Mehmet Kaynak received the B.S. degree from the Electronics and Communication Engineering Department, Istanbul Technical University, Istanbul, Turkey, in 2004, the M.S. degree from the Micro-electronic Program, Sabanci University, Istanbul, in 2006, and the Ph.D. degree from the Technical University of Berlin, Berlin, Germany, in 2014.

He joined the Technology Group, IHP Microelectronics, Frankfurt (Oder), Germany, in 2008. From 2008 to 2015, he led MEMS development at IHP. Since 2015, he has been the Head of Department of

Technology, IHP. He is also currently an Adjunct Professor with Sabanci University, Istanbul.



Ruonan Han (S'10–M'14) received the B.Sc. degree in microelectronics from Fudan University, Shanghai, China, in 2007, the M.Sc. degree in electrical engineering from the University of Florida, Gainesville, FL, USA, in 2009, and the Ph.D. degree in electrical and computer engineering from Cornell University, Ithaca, NY, USA, in 2014.

In 2012, he was an Intern with Rambus Inc., Sunnyvale, CA, USA. He is currently an Assistant Professor with the Department of Electrical Engineering and Computer Science, Massachusetts

Institute of Technology, Cambridge, MA, USA. His current research interests include microelectronic circuits and systems operating at millimeter-wave and terahertz frequencies.

Dr. Han is a member of the IEEE Solid-State Circuits Society and the IEEE Microwave Theory and Techniques Society. He was a recipient of the Cornell ECE Directors Ph.D. Thesis Research Award, the Cornell ECE Innovation Award, two best student paper awards of the IEEE Radio-Frequency Integrated Circuits Symposium in 2012 and 2017, the IEEE Microwave Theory and Technique Society Graduate Fellowship Award, the IEEE Solid-State Circuits Society Predoctoral Achievement Award, and the National Science Foundation CAREER Award in 2017. He currently holds the MIT E. E. Landsman (1958) Career Development Chair Professorship. He serves on the Technical Program Committee of the IEEE RFIC Symposium and the Steering Committee of the 2019 IEEE International Microwave Symposium.